

HI gas content of SDSS galaxies revealed by ALFALFA: implications for the mass-metallicity relation and the environmental dependence of HI in the local Universe

Ying Zu¹★,

¹*Department of Astronomy, Shanghai Jiao Tong University, Shanghai 200240, China*

Accepted XXX. Received YYY; in original form ZZZ

ABSTRACT

The neutral hydrogen (HI) gas is an important barometer of recent star formation and metal enrichment activities in galaxies. I develop a novel statistical method for predicting the HI-to-stellar mass ratio f_{HI} of galaxies from their stellar mass and optical colour, and apply it to a volume-limited galaxy sample jointly observed by the Sloan Digital Sky Survey and the Arecibo Legacy Fast ALFA survey. I eliminate the impact of the Malmquist bias against HI-deficient systems on the f_{HI} predictor by properly accounting for the HI detection probability of each galaxy in the analysis. The best-fitting f_{HI} predictor, with an estimated scatter of 0.272 dex, provides excellent description to the observed HI mass function. After defining an HI excess parameter as the deviation of the observed f_{HI} from the expected value, I confirm that there exists a strong secondary dependence of the mass-metallicity relation on HI excess. By further examining the 2D metallicity distribution on the specific star formation rate vs. HI excess plane, I show that the metallicity dependence on HI is likely more fundamental than that on specific star formation rate. In addition, I find that the environmental dependence of HI in the local Universe can be effectively described by the cross-correlation coefficient between HI excess and the red galaxy overdensity $\rho_{cc} = -0.18$. This weak anti-correlation also successfully explains the observed dependence of HI clustering on f_{HI} . My method provides a useful framework for learning HI gas evolution from the synergy between future HI and optical galaxy surveys.

Key words: galaxies: evolution — galaxies: formation — galaxies: abundances — galaxies: ISM — galaxies: statistics — cosmology: large-scale structure of Universe

1 INTRODUCTION

The neutral hydrogen (HI) gas represents a key intermediate stage in baryon cycling, between the initial accretion from the diffuse circumgalactic or intergalactic medium (Sancisi et al. 2008; Tumlinson et al. 2017) and the formation of dense molecular clouds that directly fuel star formation (Kennicutt & Evans 2012; Lada et al. 2012; Leroy et al. 2013). The variation of the HI gas reservoir usually precedes the colour transformation of galaxies induced by star formation and quenching (Baldry et al. 2004; Faber et al. 2007), while regulating the metallicity of the interstellar medium (ISM) together with galactic outflows (Dalcanton 2007; Matteucci 2012). In this paper, I develop a statistical framework for connecting the HI gas mass detected by ALFALFA (Haynes et al. 2011) to the stellar mass and optical colours of galaxies observed in SDSS (York et al. 2000), and explore the phys-

ical drivers of gas-phase metallicity and the environmental dependence of HI within this framework.

As the most important measure of the HI content of a galaxy, the HI-to-stellar mass ratio f_{HI} (hereafter referred to as HI fraction) has been found to correlate with the optical colour with a scatter of ~ 0.4 dex (Kannappan 2004). Subsequently, Zhang et al. (2009) built a photometric estimator of f_{HI} by introducing an additional scaling of f_{HI} with the i -band surface brightness, reducing the scatter to 0.31 dex. Li et al. (2012) later extended the f_{HI} estimator by using a linear combination of four parameters (including stellar mass, stellar surface mass density μ_* , NUV- r colour, and the $g-i$ colour gradient), resulting a slightly improved scatter of 0.3 dex and a more accurate match to the high- f_{HI} systems observed by ALFALFA. Alternatively, non-linear predictors have been recently developed using machine learning algorithms, which usually require training over a large number of HI-detected systems (Teimoorinia et al. 2017; Rafieferantsoa et al. 2018), or simple functional fits to the median

★ E-mail: yingzu@sjtu.edu.cn

f_{HI} trend with stellar mass (Maddox, et al. 2015; Calette, et al. 2018).

However, current HI surveys like ALFALFA are relatively shallow in depth, and are thus systematically biased against low- f_{HI} systems at any given redshift. Consequently, any f_{HI} predictor inferred or trained exclusively from systems above the HI detection threshold would be plagued by the Malmquist bias, overestimating the f_{HI} for systems that are missed by the HI survey. Such Malmquist bias can be partially alleviated by observing a smaller volume to a higher depth in HI. For example, using a roughly f_{HI} -limited but significantly smaller sample (GASS; GALEX Arecibo SDSS Survey), Catinella et al. (2010) constructed a f_{HI} predictor using the linear combination of NUV- r colour and μ , resulting in a scatter of ~ 0.3 dex (see also Catinella et al. 2013). Without having to trade volume for depth, we develop a new method to eliminate the Malmquist bias when predicting f_{HI} from the stellar mass and colour of SDSS galaxies, by properly accounting for the ALFALFA detection probability of each SDSS galaxy in the analysis.

Beyond f_{HI} , the metal abundance within the gas serves as the fossil record of the chemical enrichment history, reflecting the complex interplay between star formation and gas accretion during the baryon cycling (Peeples et al. 2014). For star-forming galaxies, gas-phase metallicity is tightly corrected with stellar mass in the oxygen-to-hydrogen abundance ratio, forming the well-known mass-metallicity relation (MZR; Tremonti et al. 2004). It has been suggested that the star formation rate (SFR) could drive the scatter in MZR. Ellison, et al. (2008) first reported the existence of a secondary dependence of the MZR on SFR, and Mannucci et al. (2010) later proposed that galaxies observed up to $z \sim 2.5$ define a tight surface in the 3D space of stellar mass, SFR, and gas-phase metallicity (a.k.a., the fundamental metallicity relation; FMR), with a residual dispersion of 0.05 dex in metallicity (see also Lara-López et al. 2010; Andrews & Martini 2013).

The existence of this secondary dependence, however, has been questioned by studies based on the integral field spectroscopy (IFS; Sánchez, et al. 2013; Barrera-Ballesteros, et al. 2017; Sánchez, et al. 2017, 2019), contrary to many results based on single-aperture spectroscopic surveys (Yates et al. 2012; Salim et al. 2014; Cresci, Mannucci & Curti 2019, e.g., SDSS). In particular, Sánchez, et al. (2013) claimed that the secondary relation could be explained by a pure aperture effect in the SDSS survey. Large discrepancies also persist among various studies based on the single-aperture data, which may arise from the use of different metallicity indicators (Kashino, et al. 2016) and different galaxy selection criteria adopted in different studies (Salim et al. 2014; Telford et al. 2016). Nevertheless, various theoretical models have subsequently been proposed to explain the MZR, assuming SFR is the main process that shaped the MZR (Peeples & Shankar 2011; Davé et al. 2012; Dayal et al. 2013; Lilly et al. 2013; Zahid et al. 2014).

Besides star formation, it is reasonable to expect that gas accretion plays a role in regulating the metallicity of the ISM. Indeed, Bothwell et al. (2013) showed that the MZR of ~ 4000 ALFALFA galaxies exhibits a strong secondary dependence on HI mass, with HI-rich galaxies being more metal poor at fixed stellar mass. Using 260 nearby galaxies from the *Herschel* Reference Survey, Hughes, et al. (2013)

detected a similar anti-correlation between gas fraction and oxygen abundance at fixed stellar mass, but almost no environmental dependence of the MZR. Applying a principal component analysis over ~ 200 galaxies compiled from several molecular gas surveys, Bothwell et al. (2016b) further argued that the underlying driver of MZR is the molecular gas mass, and the FMR is merely a by-product of molecular FMR via the Kennicutt-Schmidt law (Bothwell et al. 2016a). More recently, by stacking the HI spectra of star-forming galaxies along the MZR, Brown et al. (2018) confirmed the strong anti-correlation between HI mass and gas-phase metallicity at fixed stellar mass, providing further evidence that the scatter in the MZR is primarily driven by fluctuations in gas accretion. To ascertain whether SFR or HI mass is the more fundamental driver, I will present a comprehensive analysis of metallicity, SFR, and HI mass for a large sample of galaxies jointly observed by SDSS and ALFALFA.

In addition to the optical properties of each galaxy, the HI gas reservoir also depends on the large-scale density environment. For example, it is long known that satellite galaxies in massive halos are deficient in HI (Haynes et al. 1984; Boselli & Gavazzi 2006; Yoon & Rosenberg 2015; Jaffé et al. 2015), due to processes like the ram-pressure and tidal stripping (Gunn & Gott 1972; Merritt 1983; Moore et al. 1996; Abadi et al. 1999; McCarthy et al. 2008; Kronberger et al. 2008; Bekki 2009). Gas accretion history may be tied to the halo growth history, which is known to be correlated with the large-scale environment (Fakhouri & Ma 2010). The environmental dependence of cosmic HI distribution can be predicted using semi-analytic models (Fu et al. 2010; Xie et al. 2018) and hydro-dynamic simulations (Davé et al. 2017), or statistically accounted for within the halo model (Guo et al. 2017; Obuljen et al. 2018). However, a quantitative description of the environmental dependence of HI is still lacking. In my analysis, I quantify this dependence using the cross-correlation coefficient ρ_{cc} between HI excess and galaxy overdensity, and develop three independent approaches to measuring ρ_{cc} directly from data.

This paper is organized as follows. I briefly describe the data and the joint SDSS-ALFALFA sample in § 2, and introduce my likelihood model in § 3. I present my main findings on the mass-metallicity relation in § 4 and the environmental dependence of HI in § 5. I conclude by summarizing my results and looking to the future in § 6.

Throughout this paper, I assume the *WMAP9* cosmology (Hinshaw et al. 2013) for distance calculations. All the length and mass units in this paper are scaled as if the Hubble constant were $100 \text{ km s}^{-1} \text{ Mpc}^{-1}$. In particular, all the separations are co-moving distances in units of $h^{-1} \text{ Mpc}$, and the stellar and HI mass are both in units of $h^{-2} M_{\odot}$. I use $\lg x = \log_{10} x$ for the base-10 logarithm.

2 DATA

2.1 SDSS Volume-Limited Stellar Mass Sample

I make use of the final data release of the Sloan Digital Sky Survey (SDSS DR7; York et al. 2000; Abazajian et al. 2009), which contains the completed data set of the SDSS-I and the SDSS-II. In particular, I obtain the Main Galaxy Sample (MGS) data from the *dr72* large-scale structure sample

bright0 of the “New York University Value Added Catalogue” (NYU-VAGC), constructed as described in Blanton et al. (2005). The **bright0** sample includes galaxies with $10 < m_r < 17.6$, where m_r is the r -band Petrosian apparent magnitude, corrected for Galactic extinction. I apply the “nearest-neighbour” scheme to correct for the 7% galaxies that are without redshift due to fibre collision, and use data exclusively within the contiguous area in the North Galactic Cap and regions with angular completeness greater than 0.8.

I employ the stellar mass and gas-phase metallicity estimates from the latest MPA/JHU value-added galaxy catalogue¹. The stellar masses were estimated based on fits to the SDSS photometry following the philosophy of Kauffmann et al. (2003a) and Salim, et al. (2007), and assuming the Chabrier (Chabrier 2003) initial mass function (IMF) and the Bruzual & Charlot (2003) SPS model. The MPA/JHU stellar mass catalogue is then matched to the NYU-VAGC **bright0** sample. For the gas-phase metallicities of galaxies, I adopt the Bayesian metallicity estimates from fitting to multiple strong nebula emission lines (Tremonti et al. 2004).

From the **bright0** catalogue, I select a volume-limited sample of 14,140 galaxies with log-stellar mass $\lg(M_*/h^{-2}M_\odot) \geq 9.4$ and redshift range $z \in [0.016, 0.04]$, which forms the basis sample for my joint analysis with ALFALFA (as will be described below). Although the ALFALFA survey robustly detected HI sources up to $z \sim 0.05$ before encountering the radio frequency interference (RFI), I choose a slightly lower redshift limit of $z_{\max} = 0.04$ so that the volume-limited sample can reach a lower threshold in stellar mass, hence a higher fraction of HI detections within the SDSS sample.

2.2 The ALFALFA $\alpha.100$ HI Sample

The Arecibo Fast Legacy ALFA (ALFALFA; Haynes et al. 2011) survey is a blind extragalactic HI survey conducted using the seven-horn Arecibo L-band Feed Array (ALFA) onboard the 305-m Arecibo telescope. In order to reveal the faint-end population of the HI mass function in the local Universe ($z < 0.05$), ALFALFA mapped ~ 7000 deg² of two contiguous high Galactic latitude regions between 2005 and 2011, searching for HI line emission across the entire frequency range between 1335 and 1435 MHz. I make use of the final data release ($\alpha.100^2$; Haynes et al. 2018), which contains ~ 31500 sources up to $z = 0.06$. Due to the minimal overlap between the ALFALFA and SDSS footprints in the southern Galactic cap, I will focus exclusively on the northern Galactic region in my joint analysis of the two surveys.

Each HI detection is characterised by its angular position on the sky, radial velocity, velocity width W_{50} , and integrated HI line flux density S_{21} . The HI mass of each system can be estimated as

$$M_{\text{HI}} = 2.356 \times 10^5 D^2 S_{21} [h^{-2} M_\odot], \quad (1)$$

where D is the distance to the source measured in units of h^{-1} Mpc, and S_{21} in units of Jy km s^{-1} . Each detection is then assigned a detection category code depending on several reliability indicators, including the signal-to-noise ratio (S/N)

¹ <http://home.strw.leidenuniv.nl/~jarle/SDSS/>

² <http://egg.astro.cornell.edu/alfalfa/>

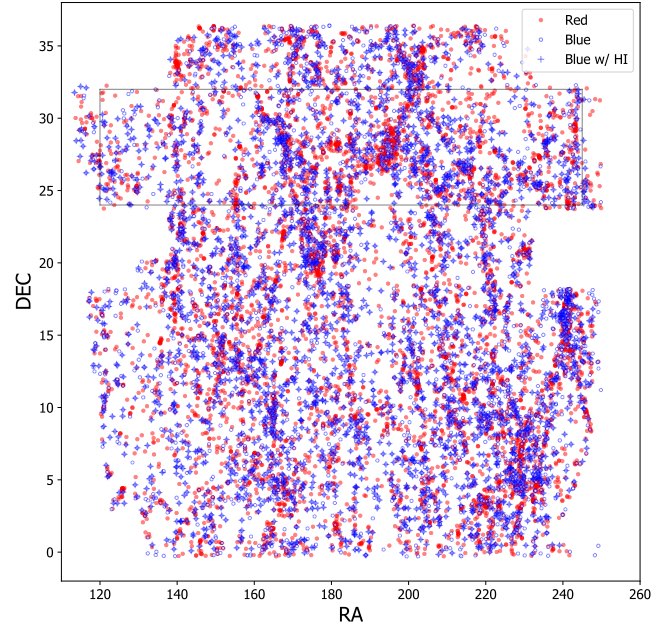


Figure 1. The overlapping footprint between SDSS and ALFALFA in the northern galactic cap. Red filled and blue open circles indicate the red and blue galaxies observed by SDSS, respectively. Blue galaxies that are detected in ALFALFA are additionally marked by blue crosses. The SDSS sample is volume-limited with $\lg(M_*/h^{-2}M_\odot) \geq 9.4$ and $z \in [0.016, 0.04]$. The region enclosed by the rectangular box is further highlighted in Figure 2.

of the detection and whether there exists an optical counterpart identified in other surveys (mainly SDSS). In particular, the “Code 1” sources (25434) are reliable detections with S/N above 6.5, while a subset of those below 6.5 are assigned “Code 2” (6068) due to having identified optical counterparts. In general, the Code 2 detections are also highly reliable despite having a relatively low S/N. Therefore, I will include both categories of detections in my analysis, and develop a likelihood model to self-consistently account for the non-detections.

2.3 Cross-matched SDSS and ALFALFA Sample

To study the HI content of optically selected galaxies, I cross-match the SDSS **bright0** and the ALFALFA $\alpha.100$ catalogues across their shared footprint in the northern Galactic cap. For each SDSS galaxy I first find all its potential HI counterparts by adopting a search radius of 36 arcsec, 80% larger than the typical centroiding uncertainty of ALFALFA (~ 20 arcsec; Haynes et al. 2011). I flag it as an HI non-detection if no ALFALFA source is found within 36 arcsec of that galaxy; If the search returns one or multiple HI candidates, I then examine if the radial velocity of each candidate falls within $\pm 600 \text{ km s}^{-1}$ of the SDSS redshift. To ensure that the match is unique, I always choose the closest HI source (in 2D) when there are multiple candidates left after the two passes.

After the cross-match, each SDSS galaxy in the volume-limited stellar mass sample described in §2.1 is either detected in ALFALFA with a reliable HI mass, or an HI non-

detection due to the lack of an HI emission with S/N above 6.5. For each SDSS galaxy detected in HI, I characterise the HI richness of the system by defining an HI-to-stellar mass ratio $f_{\text{HI}} \equiv M_{\text{HI}}/M_*$, which I refer to as *HI fraction* throughout the rest of the paper. For the galaxies that are not detected in HI, I emphasize that the resulting Malmquist bias not only has to be properly accounted for in the analysis, but they should also provide important clues as to which kind of SDSS galaxies (in terms of M_* and $g-r$) are intrinsically more likely to be HI-deficient than those that are observed.

It is worth nothing that, the spectroscopic measurement of each SDSS galaxy is confined within a 3-arcsec aperture (i.e., diameter of the fiber) centred on that galaxy. To correct for this aperture effect on SFR, the *total* SFR of galaxies are derived from empirically extrapolating the *fiber* SFR using broad-band colours (Brinchmann, et al. 2004; Salim, et al. 2007). However, there is no such aperture correction available for metallicities and the ALFALFA observation has a much larger effective aperture than SDSS. The mixing of different physical scales due to the different observational apertures may introduce some spurious correlations in my joint metallicity-SFR-HI analysis. This aperture bias can be alleviated by using the same aperture for metallicity and SFR measurements with resolved spectroscopy from IFS observations, as done by Barrera-Ballesteros, et al. (2018). However, due to the lack of real HI observations with matching aperture, they had to derive gas fraction from dust extinction inferred from the optical spectra, which could lead to spurious correlations of gas fraction with both SFR and metallicity. Therefore, in order to focus on the physical processes at the disk-halo interface, I employ the aperture-corrected total SFR and the direct HI mass from ALFALFA for my analysis, and use the fiber metallicity to study the implications of those processes for the chemical enrichment in the central region of galaxies. I will return to the impact of aperture bias later in § 4.

I plan to focus on the star-forming population in my analysis, as the majority of quenched galaxies are not detected in ALFALFA and those detected in HI do not follow the same gas scaling relations as the star-forming ones (Boselli et al. 2014). Therefore, I divide galaxies into quenched (red) and star-forming (blue) based on their $g-r$ colours (k -corrected to $z=0.1$). I use broad-band colours rather than the star formation rate (SFR), because I am interested in building a photometric estimator of HI fraction that do not rely on high S/N spectroscopic observations. For the same reason, we did not remove the 1,650 type 2 Active Galactic Nucleus (AGN) candidates from the blue sample using the BPT diagnostics, which rely on emission line indices that usually require high S/N spectra. Following Zu & Mandelbaum (2016), we adopt a stellar mass-dependent colour cut to divide galaxies into red and blue,

$$(g-r)_{\text{cut}}(M_*) = 0.8 \left(\frac{\lg M_* [h^{-2} M_{\odot}]}{10.5} \right)^{0.6}, \quad (2)$$

indicated by the gray dashed lines in Fig. 3 (described further below).

To summarize, my volume-limited SDSS-ALFALFA joint sample includes 8,721 red and 5,419 blue galaxies with stellar mass above $\lg(M_*/h^{-2}M_{\odot}) = 9.4$ and redshifts between 0.016 and 0.04. I will focus exclusively on this joint sample throughout the rest of the paper. Figure 1 show the

distribution of red (red dots) and blue (blue circles) galaxies of my joint sample across the shared footprint between SDSS and ALFALFA. Among the 5,419 blue galaxies, 3,258 (60%) of them were detected in HI by ALFALFA (blue crosses; including both Code 1 and 2 detections), and 2,161 are non-detection in ALFALFA, respectively. The region enclosed by the gray rectangular box is further highlighted in Figure 2, which indicates the redshift and RA distribution of red galaxies (red dots) and blue galaxies with five different levels of f_{HI} (colour-filled circles): HI non-detection (orange), $\lg f_{\text{HI}} < -0.5$ (green), $-0.5 \leq \lg f_{\text{HI}} < -0.25$ (cyan), $-0.25 \leq \lg f_{\text{HI}} < 0$ (blue), and $0 \leq \lg f_{\text{HI}} < 0.5$ (purple). The Coma cluster can be clearly seen as the dominant structure at $z \sim 0.023$ and $\text{RA} \sim 13^{\text{h}}$.

Figure 3 shows the colour-mass diagrams of eight different redshift bins ($\Delta z = 0.003$) between $z = 0.016$ and 0.04. In each panel, the red dots above the gray dashed line (Equation. 2) represent the quenched/red galaxies, while the colour-filled and blue open circles below are blue galaxies with and without detection in HI, respectively. The colour-coding of the filled circles indicate the value of $\lg f_{\text{HI}}$, as described by the colourbar shown in the top left panel. The inset panels show the observed stellar mass functions of total (gray histograms), blue (blue), and HI-detected blue (yellow) galaxies at respective redshifts. The total and blue histograms stay roughly unchanged across the eight redshift bins, a manifest of the high stellar mass-completeness of the SDSS volume-limited sample. However, the yellow histograms decrease substantially at the low mass end towards higher redshifts, signaling the strong Malmquist bias of the HI detection rate in ALFALFA.

Within the blue population shown in Figure 3, the HI non-detections mainly occupy the high- $g-r$ and low- M_* corner of the so-called “blue cloud” at low redshifts (top panels), but spread out to the entire cloud in the highest redshift bin (bottom right panel). Among the HI-detected galaxies, the HI fraction exhibits strong decreasing trends with both $g-r$ and M_* in all panels. The trend with $g-r$ is likely real, because at fixed M_* the non-detections are preferentially redder and have a smaller average M_{HI} (hence f_{HI}) than those detected in HI. However, it is unclear whether the trend with M_* seen in each panel is physical — at fixed colour the non-detections have on average lower M_* and lower M_{HI} than those detected in HI, but the two populations may have similar f_{HI} . In the next Section, I will build a rigorous likelihood model to quantify the level of intrinsic correlation between f_{HI} and M_* despite the obscuration caused by the Malmquist bias.

3 METHODOLOGY

3.1 HI Fraction Predictor and Detection Probability Model

Inspired by the two roughly independent trends of $\lg f_{\text{HI}}$ with $\lg M_*$ and $g-r$ seen in Figure 3, I construct a linear mixture model for the HI fraction predictor (HI-FP)

$$\lg f_{\text{HI}} = a \times \lg M_* + b \times (g-r) + c + \sigma_{\lg f_{\text{HI}}} \times \epsilon, \quad (3)$$

where a , b , and c are the three parameters that determine $\langle \lg f_{\text{HI}} | M_*, g-r \rangle$ (i.e., the expected value of $\lg f_{\text{HI}}$ for any

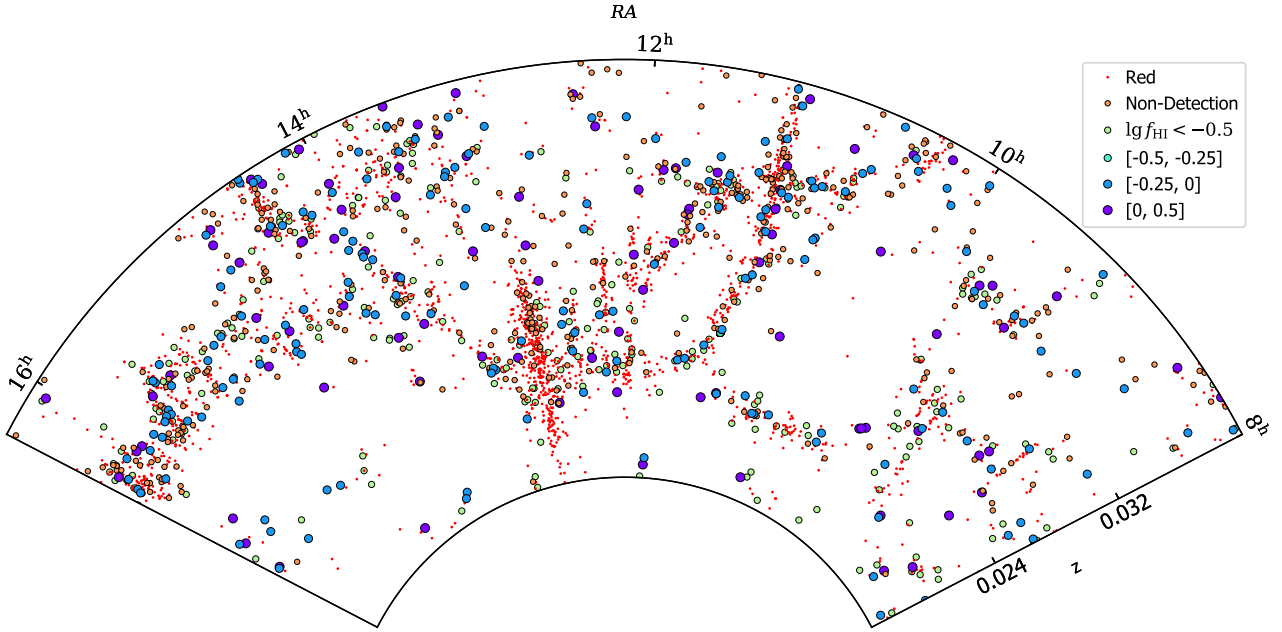


Figure 2. Redshift distribution of galaxies in the SDSS-ALFALFA joint sample ($120 < \text{RA} < 245$ and $24 < \text{DEC} < 32$; highlighted by the rectangular box in Figure 1). Red dots and coloured circles indicate the positions of the red and blue SDSS galaxies, respectively. Different sizes and colours of the circles correspond to the five levels of HI gas fraction f_{HI} observed by ALFALFA (from “non-detection” to $f_{\text{HI}} > 1$), indicated by the legend on the top right. The dominant structure at $z \sim 0.023$ and $\text{RA} \sim 13^{\text{h}}$ is the Coma cluster.

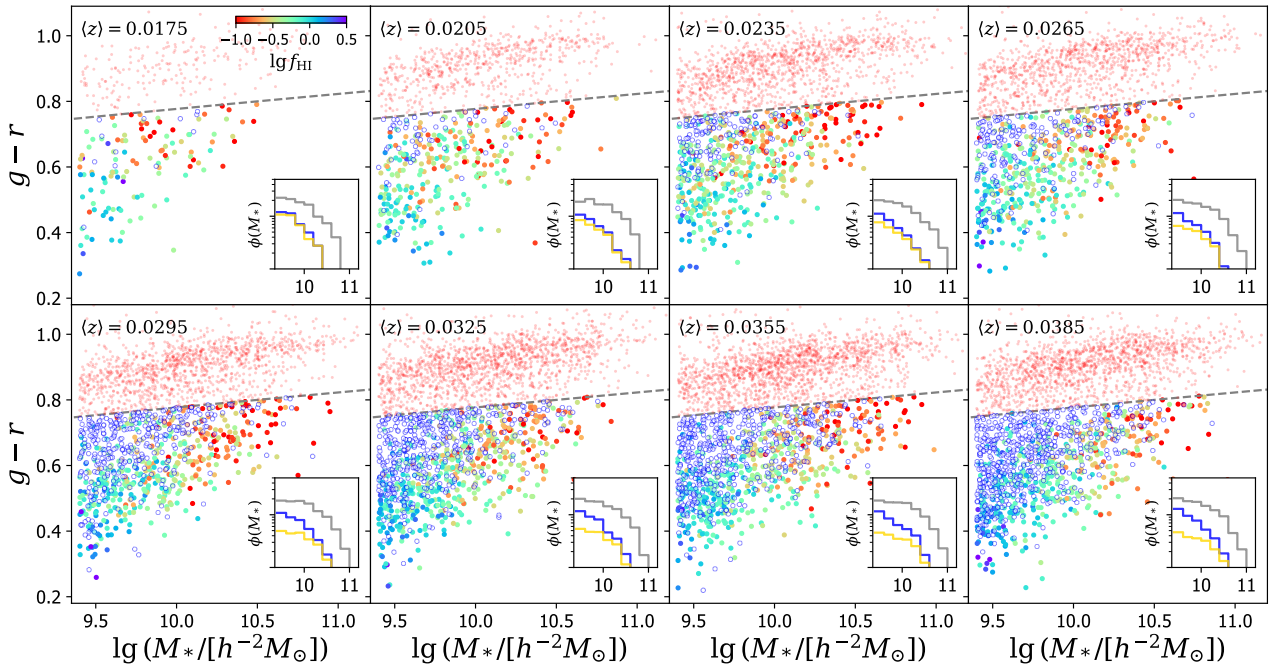


Figure 3. Colour-mass diagrams of the SDSS-ALFALFA joint sample at eight different redshift slices (between 0.016 and 0.04 with $\Delta z = 0.003$). In each panel, red dots indicate the red galaxies, defined as those above the colour cut (gray dashed line) on the diagram. Below the colour cut, blue open circles indicate the blue galaxies that are not detected in ALFALFA, while the colour-filled circles are the blue galaxies detected with different HI gas fractions f_{HI} , colour-coded by the colour bar in the top left panel. The inset panel inside each panel shows the stellar mass functions of the total (gray), blue (blue), and ALFALFA-detected blue (gold) galaxies. While the stellar mass functions of the total and blue galaxies remain unchanged with redshift, the HI-detection completeness of ALFALFA decreases rapidly with increasing redshift.

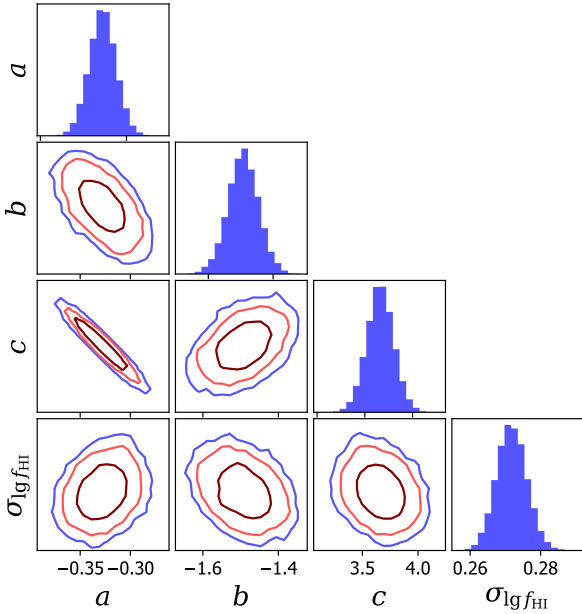


Figure 4. Parameter constraint for the HI gas fraction predictor: $\lg f_{\text{HI}} = a \lg M_* + b(g-r) + c + \epsilon \sigma_{\lg f_{\text{HI}}}$, marginalized over the six nuisance parameters that describe the detection probability as a function of HI mass and redshift. Red, magenta, and blue contours in the off-diagonal panels indicate the 68%, 95%, and 98% confidence levels, respectively.

galaxy with given M_* and $g-r$), while ϵ is a Gaussian random variable with a zero mean and a unit variance.

Note that $\sigma_{\lg f_{\text{HI}}}^2$ is the quadratic sum of the intrinsic scatter and the $1\text{-}\sigma$ measurement uncertainty. However, since the measurement error on f_{HI} reported by ALFALFA is rather uniform across the sample (~ 0.05 dex), I do not treat the two scatter components separately. In addition, I assume a constant log-normal scatter about the mean HI fraction at fixed M_* and $g-r$. I have tried incorporating redshift and stellar mass dependent scatters but failed to detect any such dependences within the data.

For the HI detection rate f_{det} , Haynes et al. (2011) demonstrated that it is mainly a function of S_{21} , modulo some dependence on W_{50} (see their Fig. 12) at fixed S_{21} , so that more extended HI emission lines are less likely to be detected. However, at fixed redshift z , I find that the observed distribution of W_{50} at fixed S_{21} only depends weakly on galaxy stellar mass and colour. Therefore, I can simply parameterise f_{det} as a function of HI mass M_{HI} ,

$$f_{\text{det}}(\lg M_{\text{HI}} | z) = \begin{cases} f(\lg M_{\text{HI}} | z) / f(12 | z) & \text{if } \lg M_{\text{HI}} \leq 12 \\ 1 & \text{if } \lg M_{\text{HI}} > 12, \end{cases} \quad (4)$$

and

$$f(\lg M_{\text{HI}} | z) = \frac{(\lg M_{\text{HI}} - 7)^{\mu_z}}{(\lg M_{\text{HI}} - 7)^{\mu_z} + (\lg M_{\text{HI},z} - 7)^{\mu_z}}, \quad (5)$$

where $\lg M_{\text{HI},z}$ is the characteristic logarithmic HI mass at which the detection rate equals to 50% at redshift z , while μ_z controls the slope of the decline from 100% at high M_{HI} to 0%

at low M_{HI} . To compute $\lg M_{\text{HI},z}$ and μ_z at arbitrary redshift z , I choose three pairs of $(\lg M_{\text{HI},z}, \mu_z)$ at $z=0.016, 0.028, 0.04$ as free parameters, and use the cubic spline (Press et al. 1992) method to smoothly interpolate the two parameters of $f_{\text{det}}(\lg M_{\text{HI}} | z)$.

Combining the HI fraction predictor and the HI detection probability model, I now have ten parameters $\theta \equiv \{a, b, c, \sigma_{\lg f_{\text{HI}}}, \lg M_{\text{HI},0}, \mu_0, \lg M_{\text{HI},1}, \mu_1, \lg M_{\text{HI},2}, \mu_2\}$, where the subscripts 0, 1, 2 indicate the three pivot redshifts 0.016, 0.028, and 0.04, respectively. Among the ten parameters, $a, b, c, \sigma_{\lg f_{\text{HI}}}$ are my key parameters that describe the HI fraction predictor, while the rest are nuisance parameters for characterising the HI incompleteness within the stellar mass-complete sample.

3.2 Likelihood Model

My input data \mathcal{D} consist of $N=5,419$ blue galaxies in the SDSS-ALFALFA joint sample, each observed with three features $\{M_*, g-r, z\}$. Among the N galaxies, $n=3,258$ of them are observed with reliable HI fraction f_{HI} , while the rest $N-n$ are non-detections. My goal is to derive the posterior probability distribution function (PDF) of θ given \mathcal{D} , $P(\theta | \mathcal{D})$, i.e., the product of the likelihood function $P(\mathcal{D} | \theta)$ and the prior $P(\theta)$. I adopt flat priors on all the ten parameters in my analysis.

Armed with the models for the HI fraction predictor (Equation. 3) and the HI incompleteness (Equation. 4), I can derive the likelihood function $P(\mathcal{D} | \theta)$ analytically by decomposing it into two components,

$$P(\mathcal{D} | \theta) = P(\mathcal{D}_{\text{det}} | \theta) \times P(\mathcal{D}_{\text{non-det}} | \theta), \quad (6)$$

where

$$P(\mathcal{D}_{\text{det}} | \theta) = \prod_{i=1}^n f_{\text{det}}(\lg M_{\text{HI}}^i | z^i, \theta) P(\lg M_{\text{HI}}^i | M_*^i, g^i - r^i, \theta) \quad (7)$$

and

$$P(\mathcal{D}_{\text{non-det}} | \theta) = \prod_{j=1}^{N-n} \int_0^{\lg M_{\text{HI}}^{\text{max}}} [(1 - f_{\text{det}}(\lg M'_{\text{HI}} | z^j, \theta))] \times P(\lg M'_{\text{HI}} | M_*^j, g^j - r^j, \theta) d \lg M'_{\text{HI}} \quad (8)$$

describe the n HI-detected galaxies and the $N-n$ non-detections, respectively. In the above equations, $P(\lg M_{\text{HI}} | M_*, g-r, \theta)$ is the probability distribution of a galaxy having a log-HI mass $\lg M_{\text{HI}}$ given its stellar mass and colour, and can be calculated as

$$P(\lg M_{\text{HI}} | M_*, g-r, \theta) = \frac{1}{\sqrt{2\pi}\sigma_{\lg f_{\text{HI}}}} \times \exp\left\{-\frac{[\lg M_{\text{HI}} - \lg M_* - a \lg M_* - b(g-r) - c]^2}{2\sigma_{\lg f_{\text{HI}}}^2}\right\}. \quad (9)$$

For computing the likelihood for the non-detections in Equation 8, I adopt an integration limit of $\lg M_{\text{HI}}^{\text{max}}=12$, consistent with the parameterisation of detection rate in Equation 4.

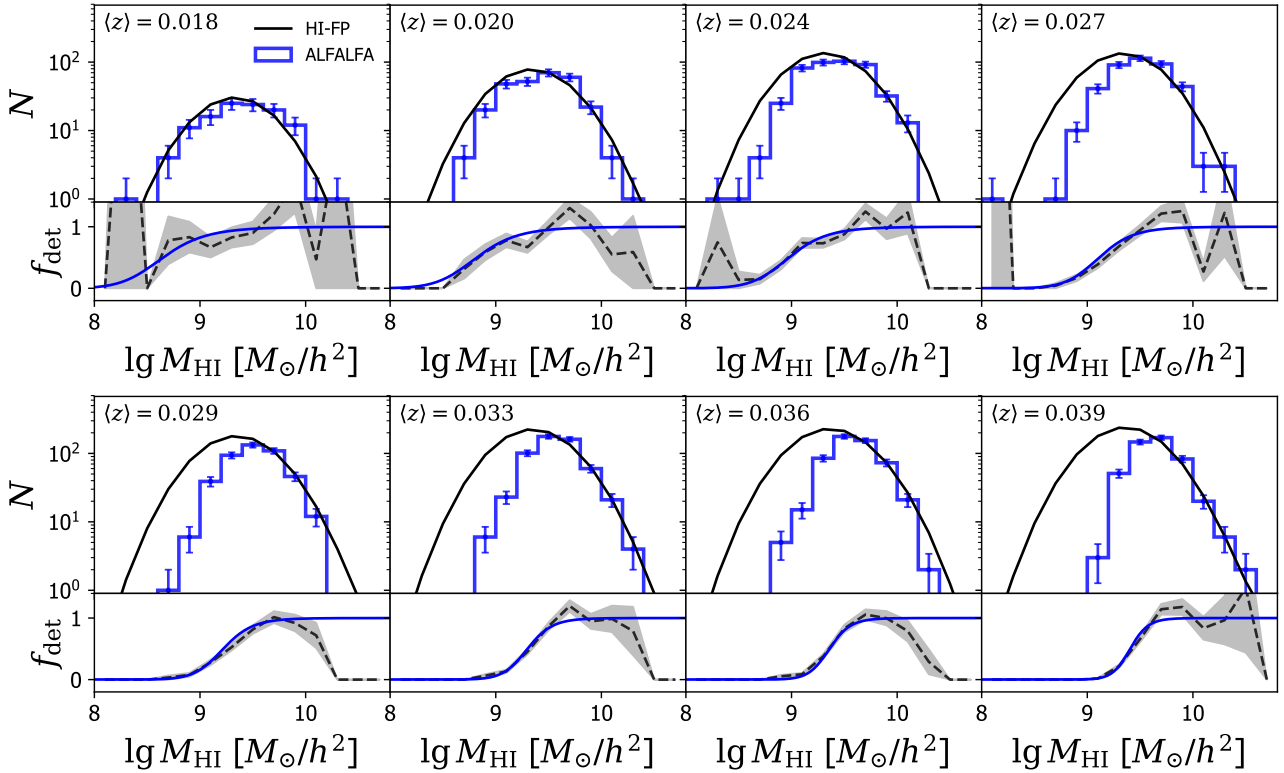


Figure 5. Comparison between the observed (blue histograms) and predicted (black curves) HI mass functions at eight different redshift slices (top sub-panels). In each bottom sub-panel, the black dashed curve shows the ratio between the observed and predicted HI mass functions, i.e., the HI-detection probability of ALFALFA in that redshift slice, with the gray shaded region indicating the Poisson uncertainties; The blue solid curve indicates the detection probability predicted from the best-fitting model.

3.3 Posterior Results

I apply the likelihood model to the SDSS-ALFALFA joint blue galaxy sample, and infer the posterior distributions of the ten parameters using the Markov Chain Monte-Carlo (MCMC) method `emcee` (Foreman-Mackey et al. 2013). After marginalizing over the six nuisance parameters that describe the HI detection rate, I obtain the posterior PDFs of the four key parameters that determine the HI fraction predictor (a , b , c) and the log-normal scatter $\sigma_{\lg f_{\text{HI}}}$, as shown in Figure 4.

The diagonal panels of Figure 4 show the marginalized 1D posterior PDFs for each of the four key parameters, and the $1-\sigma$ constraints are $a = -0.328 \pm 0.015$, $b = -1.492 \pm 0.046$, $c = 3.662 \pm 0.139$, and $\sigma_{\lg f_{\text{HI}}} = 0.272 \pm 0.004$, respectively. In the off-diagonal panels, the red, magenta, and blue contour lines enclose the 68%, 95%, and 98% confidence regions, respectively. The strong correlation between a and c indicates that the model could potentially explain away some of the apparent trend of f_{HI} with M_* by invoking a strong Malmquist bias, but the fact that $P(a|\mathcal{D})$ diminishes rapidly to zero around $a = -0.28$ demonstrates that a negative intrinsic correlation between f_{HI} and M_* at fixed $g-r$ is still necessary for interpreting the data.

I simultaneously derive $1-\sigma$ constraints on the six nuisance parameters that describe the HI detection probability (not shown on Figure 4), including $\lg M_{\text{HI},0} = 8.564 \pm 0.054$,

$\mu_0 = 7.463 \pm 1.810$, $\lg M_{\text{HI},1} = 9.170 \pm 0.010$, $\mu_1 = 14.386 \pm 0.920$, $\lg M_{\text{HI},2} = 9.427 \pm 0.013$, and $\mu_2 = 30.822 \pm 2.270$.

From the best-fitting key parameters, we can predict the underlying HI mass function of the volume-limited sample by summing the probability distribution of HI mass of all galaxies in the sample. The results for eight different redshift bins are shown as the black solid curves in Figure 5. In comparison, blue histograms with errorbars are the *observed* HI mass functions from ALFALFA. The ratios between the histograms and the solid curves, i.e., the inferred detection rate, are shown as the gray dashed lines (with shaded uncertainty bands) in the bottom sub-panels, while the blue solid curves are the predictions from the best-fitting detection rate parameters.

At the lowest redshift (top left of Figure 5; $\langle z \rangle = 0.018$), the observed HI source number counts are in good agreement with the model prediction above $\lg M_{\text{HI}} > 8.5$, indicating that ALFALFA is capable of detecting most of the galaxies with $\lg M_* > 9.4$ as HI sources. As the redshift increases (from left to right, top to bottom), the ALFALFA survey missed progressively more and more HI-rich systems — at $z = 0.04$ (bottom right), ALFALFA only detected the most HI-rich systems and is highly incomplete at $\lg M_{\text{HI}} < 9.5$.

Figure 6 provides a more visually-appealing way of showing the impact of Malmquist bias on ALFALFA detections in eight different redshift bins. In Figure 6, I compare the expected distribution that would be recovered when comparing the observed f_{HI} vs. the one predicted by my best-

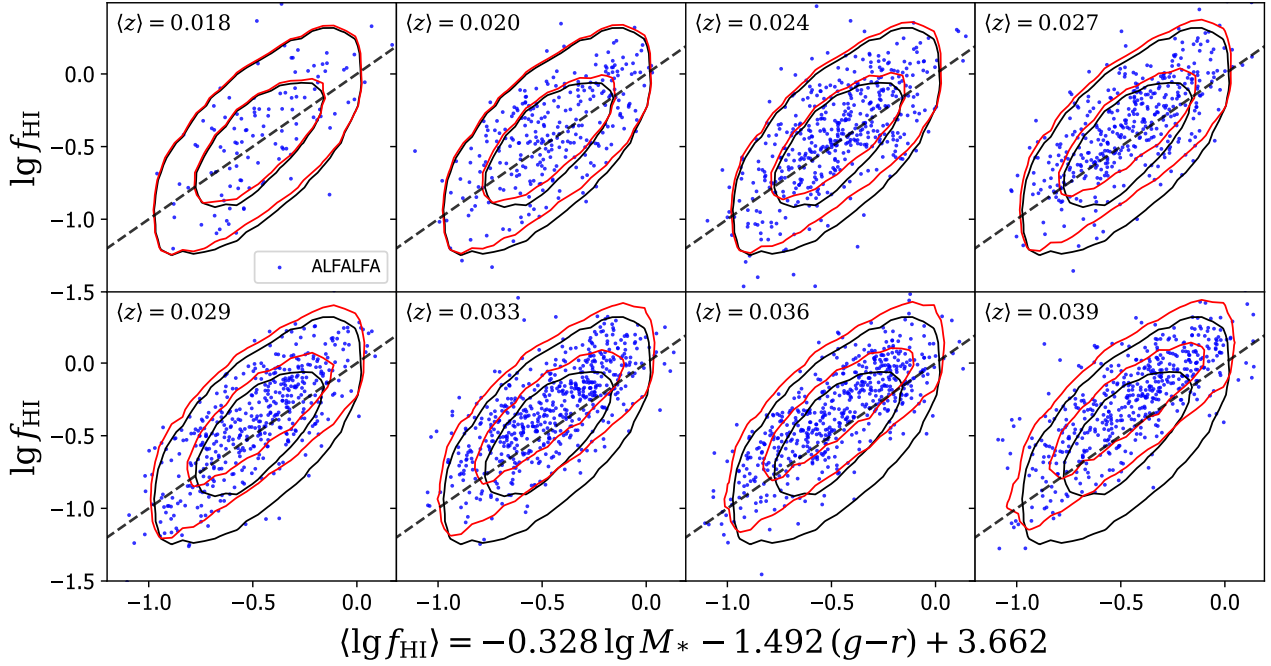


Figure 6. Comparison between the observed and predicted HI gas fractions for the joint SDSS-ALFALFA sample in eight different redshift slices. In each panel, black contours (50% and 90%) indicate the predicted galaxy distribution on the f_{HI} vs. $\langle f_{\text{HI}} \rangle$ plane of all the SDSS galaxies in the sample, while red contours show the predicted distribution of HI-detections by ALFALFA. Blue dots indicate the observed f_{HI} in ALFALFA vs. their expected value $\langle f_{\text{HI}} \rangle$. The best-fitting HI fraction predictor for $\langle f_{\text{HI}} \rangle$ is shown at the bottom of the figure. The gray dashed line is the one-to-one line of $f_{\text{HI}} = \langle f_{\text{HI}} \rangle$.

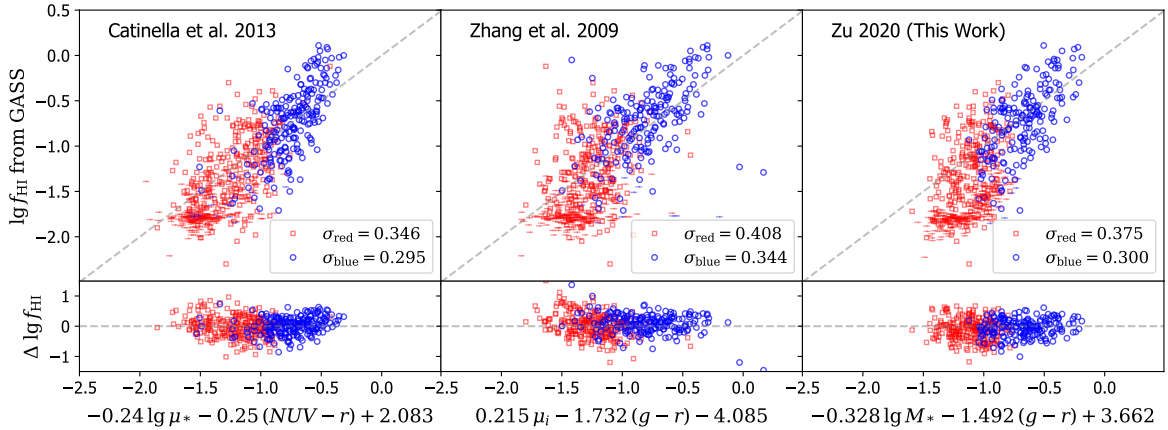


Figure 7. Comparison of the f_{gas} estimators derived by Catinella et al. (2013) (left), Zhang, et al. (2019) (middle), and this work, using the f_{gas} -limited data from the GASS reference sample. In each upper panel, blue circles and red squares indicate the HI-detected blue and red galaxies, respectively. The horizontal bars indicate the upper limits of f_{gas} for galaxies without robust HI detections. The scatters for the red and blue galaxies are shown by the legend in the bottom right. The differences between the observed and expected f_{gas} values are shown in the lower panels.

fitting model based on a pure random distribution around the best-fitting estimator,

$$\langle \lg f_{\text{HI}} \rangle = -0.328 \lg M_* - 1.492(g-r) + 3.662, \quad (10)$$

with a scatter of $\sigma_{\lg f_{\text{HI}}} = 0.272$ dex. For doing so I create a Monte Carlo simulation of f_{HI} using as input the M_* and $g-r$ colours from my SDSS sample, deriving the $\langle \lg f_{\text{HI}} \rangle$ based on Equation 10, and adding random noise. I repeat the process 100 times to recover the expected distribution, which is

shown as the black contours in each panel (50% and 90%). Then, for each of the eight redshift bins, I compare with the actual distribution of observed f_{HI} (detected by ALFALFA; blue dots) along the expected distributions based on my best-fitting detection probability at that redshift (red contours). The difference between the black and red contours is entirely due to the Malmquist bias.

In each panel, the ALFALFA-detected galaxies (blue dots) show great agreement with the model prediction (red

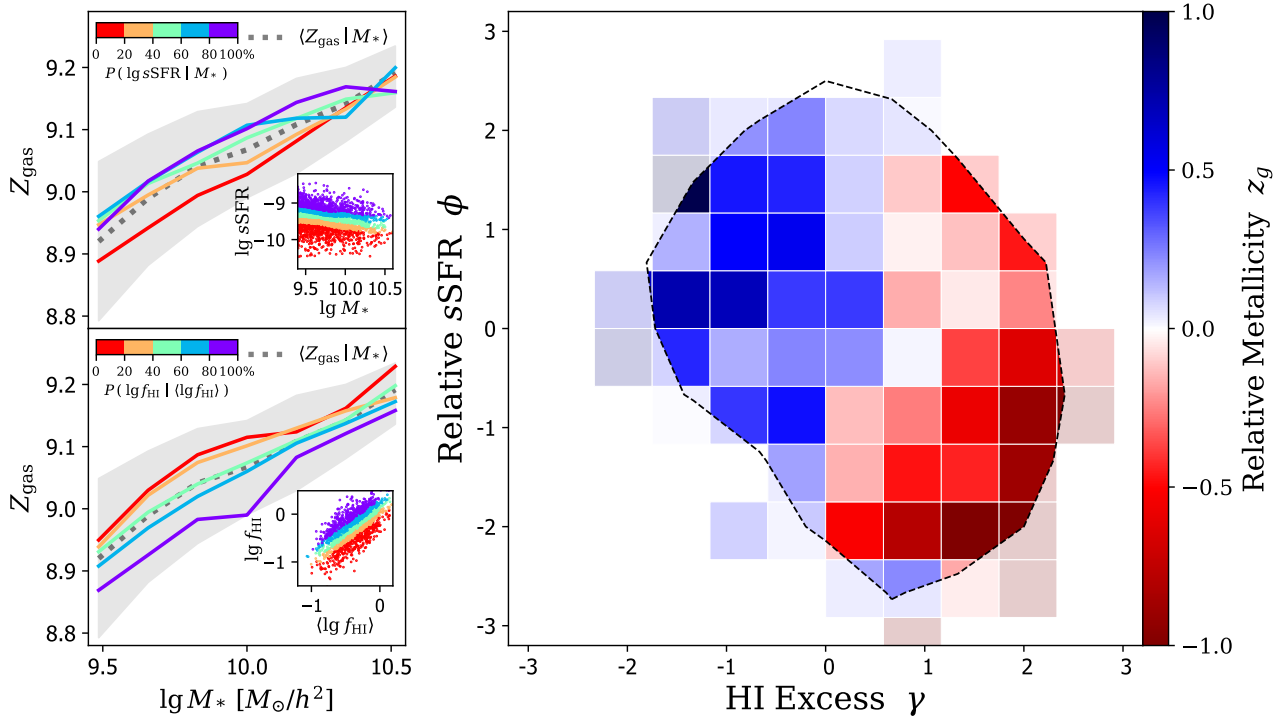


Figure 8. Top left: Dependence of the mass-metallicity relation (MZR) on specific star formation rate. The inset panel shows the distribution of galaxies on the $sSFR-M_*$ diagram, with each quintile colour-coded by the colour bar on the top left corner. The MZR of each quintile is indicated by the curve of the same colour in the main panel. The gray dotted curve and the shaded band indicate the median MZR and the scatter, respectively. Bottom left: Similar to the top left panel, but for the dependence of MZR on HI excess. Right: Distribution of the average relative metallicity Z_{gas} (normalized by the scatter in the MZR; indicated by the vertical colour bar on the right) on the relative $sSFR$ (ϕ) vs. HI excess (γ) plane. The dashed contour highlights the high number density region that encloses 90% of the sample. Clearly, the variation of relative metallicity Z_{gas} across the 2D plane is primarily driven by changes in the HI excess γ .

contours). At low redshifts ($z < 0.02$), the red contours are very similar compared to the black ones, but land primarily above the one-to-one line (dashed line) at high redshifts ($z > 0.03$) — ALFALFA preferentially detected galaxies that have excess HI mass than expected. Without correctly accounting for the Malmquist bias in the ALFALFA data, one would derive an HI fraction predictor that systematically over-predicts the average HI mass in galaxies (by more than 0.15 dex at $z \sim 0.04$). Such Malmquist bias correction is likely important for studies that utilize the HI mass function to infer the HI-to-halo mass relation (HIHM) using abundance matching techniques (Padmanabhan & Kulkarni 2017).

One way to test the accuracy of my method is to observe the f_{HI} for a subsample of the galaxies that are undetected in ALFALFA, and compare to the predictions by Equation 10. The GASS Reference Sample (DR3; Catinella et al. 2013) provides an ideal data set for such a test, as include ~ 800 galaxies that are observed to a limiting HI fraction of $f_{\text{HI}} = 2 - 5\%$, much lower than that of the ALFALFA survey. I apply my f_{HI} predictor to the f_{HI} -limited the GASS Reference Sample, and compare my estimator with two other similar methods from Catinella et al. (2013) (left) and Zhang et al. (2009) (middle) in Figure 7. In each panel, the red square and blue circles show the distributions of the red and blue galaxies (split by Equation 2), respectively, on the observed vs. predicted f_{HI} plane. The scatters of the f_{HI} estimator for red and blue galaxies are listed by legend in

the bottom right corner, while the horizontal bars clustered around $f_{\text{HI}} \sim 2\%$ indicate the upper limits for galaxies without robust HI detections. In the lower panels, I show the differences between the observed and predicted f_{HI} for the HI-detected systems. Similar to Equation 10, the Catinella et al. (2013) and Zhang et al. (2009) estimators are both linear f_{HI} predictors that rely on two photometric observables. As indicated by the axis labels of the lower panels, the Catinella et al. (2013) estimator is the linear combination of the surface stellar mass density μ_* and the NUV- r colour, while the Zhang et al. (2009) method relies on the surface brightness in i -band μ_i and the $g-r$ color. I do not compare to linear models that utilize three or more observables (e.g., Li et al. 2012) or non-linear models (e.g., Teimoorinia et al. 2017; Rafeferantsoa et al. 2018), due to the difficulty in evaluating their performances relative to mine.

The right panel of Figure 7 shows that my estimator provides a great description of the GASS galaxies, regardless of their f_{HI} or colour. In particular, the scatter of my estimator for the blue galaxies (0.3 dex) is comparable to the that of Catinella et al. (2013) (0.295 dex), which is a direct fit to the GASS data. Although Equation 10 is derived from blue galaxies only, it still does a decent job describing the HI gas fraction of the red galaxies, with a scatter (0.375 dex) only slightly higher than Catinella et al. (2013) (0.346 dex). Interestingly, the Catinella et al. (2013) estimator is biased high at both the low and high f_{HI} ends, probably

because the blue and red galaxies do not exhibit the same HI gas dependences on the surface mass density and NUV-r colour. In contrast, my estimator is unbiased across all the entire range of f_{HI} . The Zhang et al. (2009) estimator has significantly larger scatters than the other two estimators, due to the presence of several outliers. Overall, Figure 7 demonstrates the efficacy of my estimator in mitigating the Malmquist bias and predicting the HI gas mass for not only the high- f_{HI} systems, but also for the enormous number of low- f_{HI} galaxies that largely evade the detections of modern HI surveys.

Finally, for any given galaxy with observed stellar mass and colour, I can now predict the expected value of its HI mass fraction (Equation 10) that is statistically consistent with the overall abundance of HI galaxies detected and *missed* by ALFALFA. Beyond the mean HI fraction, the inferred amount of scatter (0.272 dex) is dominated by the intrinsic scatter, as the contribution from measurement uncertainties is very small (~ 0.05 dex). This intrinsic scatter ($\sqrt{0.272^2 - 0.05^2} = 0.267$ dex) was driven by a myriad of physical processes involved in the build-up and depletion of individual HI reservoir, which were inevitably linked to the galactic chemical evolution and the large-scale density environment. Therefore, I will explore the connection between HI and the gas-phase metallicity and red galaxy overdensity in the next two sections.

4 WHAT DRIVES THE MASS-METALLICITY RELATION?

4.1 Relative Metallicity, Relative sSFR, and HI Excess

The mass-metallicity relation (MZR) is a tight scaling relationship between the stellar mass M_* and the gas-phase metallicity Z_{gas} of star-forming galaxies, with a scatter of ~ 0.1 dex in the distribution of Z_{gas} at fixed M_* . Defined as $Z_{\text{gas}} \equiv 12 + \lg(\text{O}/\text{H})$, Z_{gas} is essentially a measure of the oxygen to hydrogen number density ratio in the ISM. Therefore, at fixed M_* , a galaxy can be perturbed away from the median MZR either by varying the oxygen abundance in the ISM via star formation and galactic outflow, or by modifying the gas reservoir via gas inflow and stripping. To gain more insight on the physical driver of the MZR, I will adopt this perturbative viewpoint and measure the variation of metallicity with small changes in SFR and HI gas fraction.

The star-forming galaxies also form a relatively narrow sequence on the $\lg \text{sSFR} - M_*$ plane (a.k.a., star-formation main sequence; SFMS). I define the mean MZR and SFMS by spline-interpolating the median Z_{gas} and sSFR in small bins of stellar mass (0.2 dex), respectively. Taking advantage of the MZR and SFMS, I can define a *relative* metallicity z_g and a *relative* sSFR ϕ as the deviations of the observed metallicity and logarithmic sSFR from the two mean scaling relations (each normalized by the scatter at fixed M_*), respectively. Specifically, we define z_g and ϕ as follows,

$$z_g = \frac{Z_{\text{gas}} - \langle Z_{\text{gas}} | M_* \rangle}{\sigma_{Z_{\text{gas}} | M_*}}, \quad (11)$$

and

$$\phi = \frac{\lg \text{sSFR} - \langle \lg \text{sSFR} | M_* \rangle}{\sigma_{\lg \text{sSFR} | M_*}}, \quad (12)$$

where $\langle Z_{\text{gas}} | M_* \rangle$ and $\langle \lg \text{sSFR} | M_* \rangle$ are the mean MZR and SFMS, respectively. $\sigma_{Z_{\text{gas}} | M_*}$ and $\sigma_{\lg \text{sSFR} | M_*}$ are the two corresponding scatters at fixed M_* . After switching to z_g and ϕ defined above, I can now directly compare the relative amount of metals and star formation of two arbitrary galaxies, regardless of how different their stellar masses are.

Similarly, the HI fraction of star-forming galaxies follows a tight scaling relationship about the best-fitting $\langle f_{\text{HI}} \rangle$ model (Equation 10) with a scatter of $\sigma_{\lg f_{\text{HI}}} = 0.272$ dex. To quantify the tendency of a galaxy to have excess or deficit amount of HI relative to its expected value, I define an ‘‘HI excess’’ parameter γ ,

$$\gamma = \frac{\lg f_{\text{HI}} - \lg \langle f_{\text{HI}} \rangle}{\sigma_{\lg f_{\text{HI}}}}, \quad (13)$$

where f_{HI} and $\langle f_{\text{HI}} \rangle$ are the observed and expected HI-to-stellar mass ratios, respectively.

4.2 2D Relative Metallicity Map

To study the 2D dependence of z_g on ϕ and γ , I select from the SDSS-ALFALFA joint sample a subset of HI-detected galaxies that have also high S/N spectra observed by SDSS, so that each of those galaxy has all three properties (i.e., metallicity, sSFR, and HI mass) robustly measured. I eliminated the spurious metallicity measurements due to AGNs by imposing the BPT selection criteria for star-forming galaxies defined by Kauffmann et al. (2003b). After the selections, I have 1,913 galaxies in the subsample.

The left two panels of Figure 8 summarizes the individual dependences of MZR on ϕ (top left) and γ (bottom left), respectively. In each panel, the gray dotted curve and shaded band indicate the mean MZR and its scatter; The five coloured solid lines are the mean MZR of galaxies in five quintiles of ϕ (top) or γ (bottom), colour-coded by the colour bar on the top left of each panel. The two inset panels show the segregated distributions of galaxy quintiles on the SFMS diagram and the $\lg f_{\text{HI}}$ vs. $\langle \lg f_{\text{HI}} \rangle$ plane, respectively. For the MZR dependence on ϕ shown in the top left panel, the lowest- ϕ quintile exhibits the lowest average metallicity, while the metallicity trend with the four higher- ϕ quintiles are less clear. The lowest- ϕ galaxies may have insufficient star formation to chemically enrich the entire gas reservoir, or preferentially live in systems with an excess of HI gas that dilutes the metallicity. Conversely, metallicity and HI excess exhibit a strong anti-correlation in the bottom left panel, where the five MZR of the subsamples form a well-defined decreasing sequence with increasing γ . This anti-correlation can be naturally explained if HI excess is the underlying driver of MZR.

The observed metallicity trend with ϕ indicates that there exists some weak positive correlation between ϕ and z_g , in apparent contradiction with the so-called ‘‘fundamental metallicity relation’’ (FMR), which states that the gas-phase metallicity is anti-correlated with star formation rate. However, as discussed in § 1, the existence of such an anti-correlation is still under debate. In particular, the

anti-correlation appears to be absent from IFS observations (Sánchez, et al. 2013, 2017; Barrera-Ballesteros, et al. 2017; Sánchez, et al. 2019); And when detected in single-aperture observations, the shape and amplitude of the correlation depends sensitively on the metallicity estimator and galaxy selection (Salim et al. 2014; Kashino, et al. 2016; Telford et al. 2016). For example, using the same Bayesian metallicity estimator of Tremonti et al. (2004), Yates et al. (2012) found that the metallicity trend with SFR reverses its sign to a positive correlation at the high stellar mass end from an anti-correlation at the low mass, consistent with my finding in Figure 8. However, the trend disappears entirely if the metallicity estimator of Mannucci et al. (2010) is used (Salim et al. 2014). Therefore, I emphasize that despite being weaker than the metallicity trend with γ , the $sSFR$ trend seen in Figure 8 should be regarded as the maximal possible level of correlation between $sSFR$ and z_g for the relevant stellar mass range.

To understand the strong metallicity trend with γ and the lack of such a trend with ϕ , I measure the 2D relative metallicity distribution of star-forming HI galaxies on the γ vs. ϕ plane, as shown on the right panel of Figure 8. The colour of each pixel represents the average relative metallicity $\langle z_g \rangle$ at given γ and ϕ , colour-coded by the vertical colour bar on the right. The dashed contour highlights the high number density region that encloses 90% of the galaxies, revealing a weak anti-correlation between γ and ϕ . One might worry that the aperture correction in the total $sSFR$ might induce spurious correlations between γ and ϕ , as the correction was based on galaxy colors that I also employed to build the estimator for f_{HI} (hence ϕ). To test the impact of such aperture bias, I calculate the Spearman’s cross-correlation coefficient ρ_{cc} between ϕ and the aperture correction of $sSFR$, as defined by $\lg sSFR_{total}/sSFR_{fiber}$. I do not find any discernible correlation between the two quantities ($\rho_{cc} = -0.027 \pm 0.030$), therefore the effect of aperture bias in $sSFR$ can be safely ignored in Figure 8.

Clearly, the relative metallicity exhibits a strong dependence on HI excess, so that galaxies with high γ have significantly higher z_g than those with low γ , regardless of their relative $sSFR$. Conversely, the relative metallicity shows little dependence on ϕ at fixed γ , suggesting that SFR is a secondary driver of the gas-phase metallicity of a galaxy compared to the amount of excess HI gas in that system. Therefore, the lack of a clear metallicity trend with ϕ in the top left panel of Figure 8 is expected, and the lowest metallicity exhibited by the lowest- ϕ quintile can be entirely attributed to the anti-correlation between ϕ and γ , which maps the lowest- ϕ quintile galaxies to the highest- γ (hence the lowest z_g) galaxies.

To summarize, my result in Figure 8 suggests that the scatter in the MZR is primarily tied to the amount of excess HI gas in galaxies γ , rather than the relative star formation rate ϕ . It is commonly believed that the MZR is mainly shaped by the balance between metal loss due to outflows and metal production by stellar nucleosynthesis yield, both of which are tied to star formation. However, my result suggests that the dilution effect due to inflows may have played a more important role in shaping the gas-phase metallicity than the direct modification of metal abundance. Therefore, we emphasize that it is necessary to explicitly track the evo-

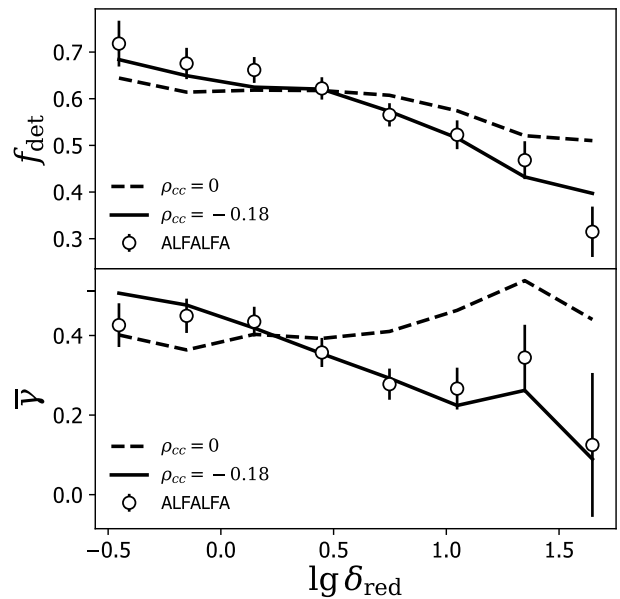


Figure 9. Top: HI detection rate as a function of δ_{red} . Open circles with errorbars show the HI detection rate in ALFALFA, while the dashed and solid lines are the predictions from two HI mocks that assume different cross-correlation coefficients between HI excess and δ_{red} , $\rho_{cc} = 0$ and -0.18 , respectively. A weak anti-correlation between HI excess and δ_{red} (-0.18) is required to reproduce the observed trend of HI detection rate with δ_{red} . Bottom: Similar as above, but for the average HI excess as a function of δ_{red} . Again, the $\rho_{cc} = -0.18$ mock successfully reproduces the ALFALFA observation.

lution of gas reservoir in the analytic or semi-analytic exploration of the MZR.

5 ENVIRONMENTAL DEPENDENCE OF HI

5.1 Red Galaxy Overdensity

My HI fraction predictor is a function of stellar mass and optical colour, without any direct dependence on the galaxy environment. Although stellar mass and colour both depends strongly on the environment, the time scale over which the environment modifies these two quantities is much longer than that of gas stripping processes. In particular, the HI gas discs of satellite galaxies can be rapidly stripped off by the ram pressure of the hot intra-cluster gas upon infall, while their star formation activities can still last for a couple Gyrs after infall (Wetzel et al. 2013; Simha et al. 2014). For those satellite galaxies, there would be no detectable change in the mass or colour of their stellar component despite a sudden drop in the HI fraction (see the paucity of HI-rich galaxies in the Coma cluster in Figure 2). Therefore, I expect that the scatter in the HI fraction predictor is at least partly driven by the galaxy environment.

Ideally, I would prefer using halo mass as the main environment indicator, as ram pressure scales with the product of the hot halo gas density and the infall velocity squared, both of which depend on halo mass. Furthermore, the observed small scatter in the so-called ‘‘Baryonic Tully-Fisher

Relation” (McGaugh et al. 2000; Lelli et al. 2016) implies that there exists a strong correlation between HI gas mass and halo mass at fixed stellar mass. However, observationally I can only measure the average halo mass for an ensemble of galaxies (Mandelbaum et al. 2016), but not yet for individual systems. Alternatively, one can employ the empirical group catalogue and estimate halo masses from the abundance matching method (AM), albeit with significant scatter between the AM and true halo masses. Using the Yang et al. SDSS group catalog, Yoon & Rosenberg (2015) found strong radial variation of the HI detection fraction inside the most massive groups. However, they failed to detect any dependence of HI fraction on the AM halo mass, likely due to the combination of scatter and poor statistics (i.e., small number of rich groups).

Inspired by the observed strong correlation between the red galaxy overdensity and halo mass (Roza & Rykoff 2014; Zu & Mandelbaum 2016, 2018), I adopt the red galaxy overdensity δ_{red} around each blue galaxy as my proxy for galaxy environment, defined as

$$\delta_{\text{red}} = \frac{N_{\text{red}}^{\text{obs}}}{N_{\text{red}}^{\text{ran}}}, \quad (14)$$

where $N_{\text{red}}^{\text{obs}}$ and $N_{\text{red}}^{\text{ran}}$ are the number counts of observed and random red galaxies within a cylindrical volume centered on that blue galaxy. The cylinder has an aperture radius $R=2h^{-1}\text{Mpc}$ and line-of-sight height $\Delta z=\pm 600\text{km s}^{-1}$. To correct for the survey masks and boundary effect when computing δ_{red} , I calculate $N_{\text{red}}^{\text{ran}}$ from a random galaxy catalogue that has the same redshift and angular selection functions as the observed red galaxy sample. The cylinder dimension is chosen roughly to match the projected radius and the Fingers-of-God effect of massive cluster. I have verified that my conclusions are insensitive to the choice of cylinder dimension.

If part of the scatter in f_{HI} is driven by δ_{red} , both the HI detection rate f_{det} and the average HI excess $\bar{\gamma}$ of blue galaxies should depend on δ_{red} , so that galaxies that live in high- δ_{red} environments are more likely to be missed by ALFALFA and have a lower $\bar{\gamma}$ than those in low- δ_{red} regions. As expected, the open circles in top and bottom panels of Figure 9 show the observed declining trend of f_{det} and $\bar{\gamma}$ with increasing δ_{red} , respectively. The dashed lines are the predictions from the null assumption that there is no dependence of γ on δ_{red} , so that the Spearman’s rank correlation coefficient ρ_{cc} between γ and δ_{red} is zero. In the $\rho_{cc}=0$ model, I randomly draw γ values from a standard normal distribution and assign mock M_{HI} values to the blue galaxies using $\lg M_{\text{HI}} = \lg M_* + (\langle \lg f_{\text{HI}} \rangle + \gamma \sigma_{\lg f_{\text{HI}}})$. I then pass the mock M_{HI} through the best-fitting detection probability model at each redshift, thereby generating a mock SDSS-ALFALFA joint sample free of any environmental dependences. Unsurprisingly, the dashed lines show no trend with δ_{red} in either panel, and the $\rho_{cc}=0$ model is thus strongly disfavored by the ALFALFA observations.

To infer the cross-correlation coefficient ρ_{cc} between γ and δ_{red} , one method is to find the value of ρ_{cc} that reproduces the observed $f_{\text{det}}(\delta_{\text{red}})$ in the top panel of Figure 9. Similarly, I generate the $\rho_{cc}<0$ mocks by imposing a negative Spearman’s rank correlation between γ and δ_{red} , while keeping the standard normal distribution of γ intact. Using a

simple minimum χ^2 estimation that takes into account the Jackknife uncertainties of f_{det} , I find that the $\rho_{cc} = -0.18$ model (solid line in the top panel) provides the best-fit to the observed $f_{\text{det}}(\delta_{\text{red}})$.

A second method for inferring ρ_{cc} is to find the best-fitting model that reproduces the observed $\bar{\gamma}(\delta_{\text{red}})$ in the bottom panel of Figure 9. I repeat a similar χ^2 fitting procedure using the $\bar{\gamma}(\delta_{\text{red}})$ data, which also yield the best-fitting value of $\rho_{cc} = -0.18$ (solid line in the bottom panel). The excellent consistency between the two independent methods of inferring ρ_{cc} is highly non-trivial, as the first method relies more on the robustness of my best-fitting detection probability model, whereas the second method depends more on the correctness of the best-fitting HI fraction predictor. Therefore, this consistency not only confirms the existence of an environmental dependence of HI in the local Universe, but also demonstrates the efficacy of my comprehensive model for interpreting the SDSS-ALFALFA joint dataset.

5.2 Clustering Dependence on f_{HI}

For a more comprehensive study of the environmental dependence of HI, I measure the projected cross-correlation functions w_p between the HI-detected galaxies and the red vs. blue galaxies in SDSS. The projected correlation function is computed as

$$w_p(r_p) = \int_{-r_p^{\text{max}}}^{r_p^{\text{max}}} \xi^s(r_p, r_\pi) dr_\pi, \quad (15)$$

where r_p and r_π are the projected and perpendicular distances between a pair of galaxies, and ξ^s is the redshift-space cross-correlation function between HI and SDSS galaxies. I adopt an integration limit of $r_\pi^{\text{max}}=40h^{-1}\text{Mpc}$ to reduce the impact due to peculiar motions. The 2D correlation function ξ^s is computed using the Davis & Peebles estimator (Davis & Peebles 1983),

$$\xi(r_p, r_\pi) = \frac{N_R}{N_D} \frac{HD}{HR} - 1, \quad (16)$$

where HD is the number count of HI-SDSS galaxy pairs separated by (r_p, r_π) , and HR is the number count of pairs between an HI-detected galaxy and a point in the SDSS random catalogue. N_D and N_R are the number of objects in the observed and random SDSS catalogues. I adopt the Davis & Peebles estimator because it only requires random catalogues for the SDSS samples, for which I have well-defined window functions and masks (but not for ALFALFA). For the SDSS galaxies, I use two separate sets of randoms for the blue and red galaxies, each with ten times the size of the observed sample. I compute the measurement uncertainties using 100 Jackknife subsamples defined over spatially contiguous patches on the sky. I refer readers to Zu & Mandelbaum (2015) for technical details in the construction of random catalogues and w_p computation.

Similarly, I also compute w_p between SDSS galaxies and the two mock HI samples constructed in § 5.1, i.e., mock ALFALFA observations assuming different levels of correlation between δ_{red} and γ ($\rho_{cc}=0$ and -0.18). The $\rho_{cc} = -0.18$ mock has shown excellent agreement with the observed $f_{\text{det}}(\delta_{\text{red}})$ and $\bar{\gamma}(\delta_{\text{red}})$ in Figure 9, but comparison between the mock and SDSS-ALFALFA w_p measurements would serve as a third and more stringent test of the $\rho_{cc} = -0.18$

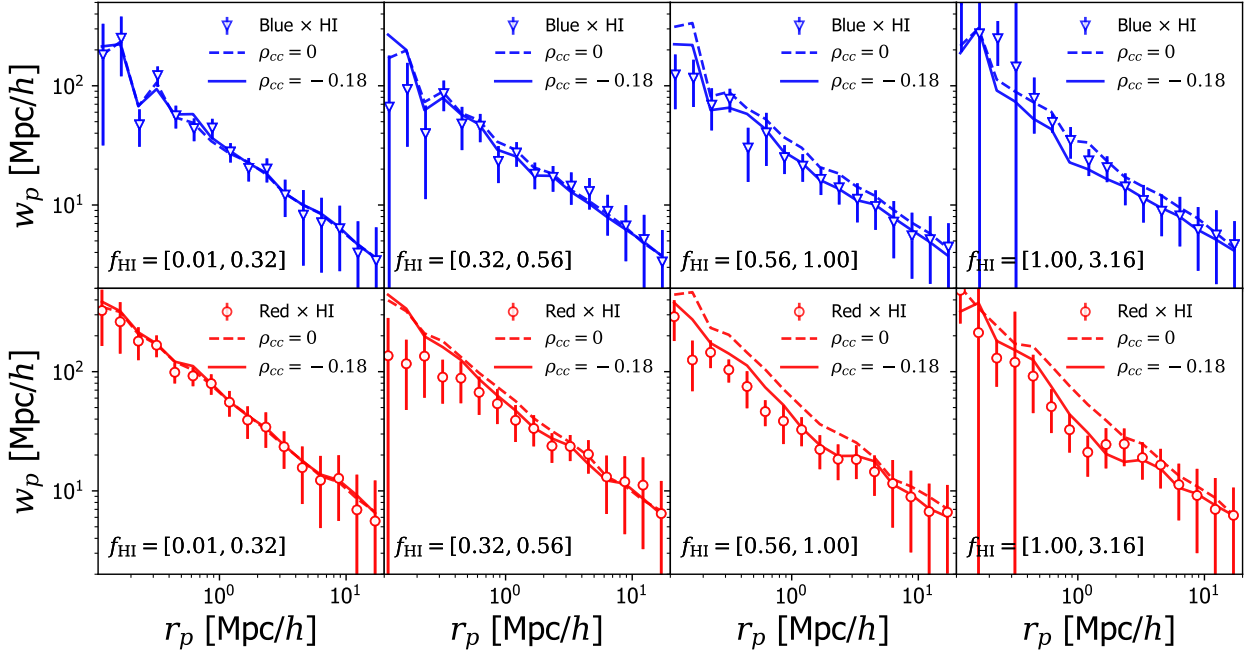


Figure 10. Projected cross-correlation functions w_p between HI-detected galaxies and the red (top row) and blue (bottom row) galaxies in SDSS. In each row, the HI-detections are divided into four bins based on their HI gas fraction f_{HI} , from HI-poor (left two panels; [0.01, 0.32], [0.32, 0.56]) to HI-rich (right two panels; [0.56, 1], [1, 3.16]). In each panel, symbols with errorbars show the w_p between SDSS red/blue galaxies and the ALFALFA detections, while the dashed and solid curves indicate the expected w_p from the two HI mocks with different cross-correlation coefficients between HI excess and δ_{red} , $\rho_{cc} = 0$ and -0.18 , respectively. The HI mock with a weak anti-correlation ($\rho_{cc} = -0.18$) successfully reproduces the observed projected correlation functions between red/blue and HI galaxies.

model — w_p directly measures the average density profile of red or blue galaxies surrounding HI galaxies on small scales ($<4h^{-1}\text{Mpc}$), as well as the clustering bias of HI galaxies on large scales ($\geq 4h^{-1}\text{Mpc}$).

Figure 10 shows the projected cross-correlation functions of blue (top row) and red (bottom row) SDSS galaxies with HI-detected galaxies in four different bins of HI fraction f_{HI} (increasing from left to right). In the top (bottom) row, blue triangles (red circles) with errorbars are the cross-correlation functions between HI and blue (red) galaxies in the SDSS-ALFALFA joint sample. In each panel, dashed and solid lines show the predictions from the $\rho_{cc}=0$ and $\rho_{cc}=-0.18$ HI mock samples, respectively. In the top panels, the mean density profile of blue galaxies around HI galaxies does not change with increasing f_{HI} , while the large-scale clustering bias of HI galaxies increases slightly with f_{HI} . The $\rho_{cc}=0$ mock (dashed lines) provides reasonable description of the w_p between blue galaxies and low HI-fraction galaxies ($f_{\text{HI}} < 0.56$), but over-predicts the amplitude of w_p on all scales for high HI-fraction systems ($f_{\text{HI}} > 0.56$). In contrast, the $\rho_{cc}=-0.18$ measurements (solid lines) of w_p are in excellent agreement with the observed cross-correlations between ALFALFA and SDSS blue galaxies in all four HI-fraction bins.

I examine the projected correlation of HI detections with the red galaxies in the bottom panels of Figure 10. In contrast to the w_p with blue galaxies, the mean density profile of red galaxies around ALFALFA galaxies shows a strong suppression for those with $f_{\text{HI}} > 0.56$ on scales below $3h^{-1}\text{Mpc}$ (compared to the dashed lines predicted by assum-

ing $\rho_{cc}=0$), consistent with having an environmental dependence of HI excess on δ_{red} . This small-scale suppression of w_p in the two high- f_{HI} bins is not captured by the $\rho_{cc}=0$ mock (dashed lines), but the feature is successfully reproduced by the $\rho_{cc}=-0.18$ mock (solid lines), showing great consistency with the two tests in Figure 9. The significant lack of red galaxies in the vicinity of high- f_{HI} systems suggests that the massive halos play an important role in driving the HI-deficient systems in dense environment, which would have otherwise been more HI-rich based on their stellar mass and colour (Equation 10).

This environmental dependence of HI is likely induced by the various stripping mechanisms in massive halos, including the tidal truncation of gas supply and the ram-pressure stripping of gaseous discs, which usually require a careful modelling of the dynamical interaction between galaxies and their host halos using semi-analytic models or hydro-dynamic simulations. However, we demonstrate that the environmental dependence of HI can be fully accounted for by assuming a cross-correlation between the HI excess γ and the red galaxy overdensity δ_{red} , and the cross-correlation coefficient ρ_{cc} can be self-consistently inferred from the data. Within the SDSS-ALFALFA joint sample, I discover that there exists a weak negative correlation between γ and δ_{red} , $\rho_{cc} = -0.18$, derived from three independent tests illustrated in Figure 9 and Figure 10. I note that this inferred correlation between γ and δ_{red} can also be used as an interesting constraint of other models of galaxy formation.

6 CONCLUSION

In this paper, I develop a statistical method to infer the HI-to-stellar mass ratio f_{HI} of galaxies from their stellar mass and optical colour, using a volume-limited galaxy sample jointly observed by SDSS and ALFALFA. Compared to the traditional methods, the key feature of my method is its capability of removing the Malmquist bias against low- f_{HI} systems in ALFALFA, via a self-consistent modelling of the HI detection rate of each galaxy observed in SDSS. The best-fitting HI fraction predictor has an estimated scatter of 0.272 dex, slightly smaller than the ~ 0.30 dex reported by traditional methods.

To explore the impact of gas accretion on gas-phase metallicity, I define an HI excess parameter γ as the deviation of the observed $\lg f_{\text{HI}}$ from the expected value (normalized by scatter). I discover a strong secondary dependence of the mass-metallicity relation on γ , echoing the findings of Bothwell et al. (2013) and Brown et al. (2018). This secondary dependence defines a fundamental metallicity relation of HI, similar to the fundamental metallicity relation of the star formation rate (Mannucci et al. 2010; Lara-López et al. 2010; Andrews & Martini 2013).

By taking advantage of two tight scaling relations, i.e., the mass-metallicity relation and the star formation main sequence, I define the relative metallicity and relative $s\text{SFR}$ of each galaxy as the (normalized) deviations from the two respective mean relations. To elucidate the underlying driver of the scatter in the MZR, I examine the 2D relative metallicity distribution on the relative $s\text{SFR}$ vs HI excess plane. I find that the variation of relative metallicity is primarily driven by the change in HI excess, so that galaxies with higher HI excesses always have lower relative metallicities, regardless of the difference in relative $s\text{SFR}$. This 2D metallicity map suggests that the metallicity dependence on HI is more fundamental than on SFR.

Furthermore, the HI excess also depends on the large-scale overdensity environment. Using the red galaxy overdensity δ_{red} as a measure of the large-scale environment, I demonstrate that there exists a weak anti-correlation between HI excess and δ_{red} in the SDSS-ALFALFA joint sample. From the dependence of detection rate and HI excess on δ_{red} , I infer the cross-correlation coefficient ρ_{cc} between the two quantities to be -0.18 . The $\rho_{cc} = -0.18$ model also successfully reproduces the dependence of HI clustering on f_{HI} . I believe this anti-correlation can be largely explained by the ram pressure and tidal stripping of HI gas discs in cluster environments (but see Wang et al. 2018).

Currently, ALFALFA is the only extragalactic HI survey of a cosmological volume (Avila, Novaes, Bernui & de Carvalho 2018). However, with the advent of exciting HI surveys like the Square Kilometer Array (SKA; Maartens et al. 2015) and the Five-hundred-meter Aperture Spherical Telescope (FAST; Nan et al. 2011), the HI sky will be observed to a much higher depth within a significantly larger volume than ALFALFA. In particular, FAST will conduct the Comensal Radio Astronomy FasT Survey (Zhang, et al. 2019, CRAFTS), a drift scan survey of ~ 600000 HI sources across 20000 deg^2 sky up to $z=0.35$. My method will provide a viable path to the synergy between the next-generation HI surveys like CRAFTS and upcoming optical surveys, e.g., the Bright Galaxy Survey program within the Dark Energy Spectro-

scopic Instrument (DESI; DESI Collaboration et al. 2016). In particular, we expect the method to provide valuable insight into the evolution of HI gas and metallicity in cluster environments (Peng & Maiolino 2014; Li et al. 2018) and the dependence of HI on large-scale tidal environments (Liao & Gao 2018; Alam et al. 2018).

ACKNOWLEDGEMENTS

I thank the anonymous referee for suggestions that greatly improved the manuscript, and Alessandro Sonnenfeld for helpful discussions. YZ acknowledges the support by the National Key Basic Research and Development Program of China (No. 2018YFA0404504), National Science Foundation of China (11621303, 11873038), the National One-Thousand Youth Talent Program of China, and the STJU start-up fund (No. WF220407220).

REFERENCES

- Abadi M. G., Moore B., Bower R. G., 1999, *MNRAS*, **308**, 947
 Abazajian K. N., et al., 2009, *ApJS*, **182**, 543
 Alam S., Zu Y., Peacock J. A., Mandelbaum R., 2018, preprint, ([arXiv:1801.04878](https://arxiv.org/abs/1801.04878))
 Andrews B. H., Martini P., 2013, *ApJ*, **765**, 140
 Avila F., Novaes C. P., Bernui A., de Carvalho E., 2018, *JCAP*, **2018**, 041
 Baldry I. K., Glazebrook K., Brinkmann J., Ivezić Ž., Lupton R. H., Nichol R. C., Szalay A. S., 2004, *ApJ*, **600**, 681
 Barrera-Ballesteros J. K., Sánchez S. F., Heckman T., Blanc G. A., MaNGA Team, 2017, *ApJ*, **844**, 80
 Barrera-Ballesteros J. K., et al., 2018, *ApJ*, **852**, 74
 Bekki K., 2009, *MNRAS*, **399**, 2221
 Blanton M. R., Eisenstein D., Hogg D. W., Schlegel D. J., Brinkmann J., 2005, *ApJ*, **629**, 143
 Boselli A., Gavazzi G., 2006, *PASP*, **118**, 517
 Boselli A., Cortese L., Boquien M., Boissier S., Catinella B., Lagos C., Saintonge A., 2014, *A&A*, **564**, A66
 Bothwell M. S., Maiolino R., Kennicutt R., Cresci G., Mannucci F., Marconi A., Cicone C., 2013, *MNRAS*, **433**, 1425
 Bothwell M. S., Maiolino R., Peng Y., Cicone C., Griffith H., Wagg J., 2016a, *MNRAS*, **455**, 1156
 Bothwell M. S., Maiolino R., Cicone C., Peng Y., Wagg J., 2016b, *A&A*, **595**, A48
 Brinchmann J., Charlot S., White S. D. M., Tremonti C., Kauffmann G., Heckman T., Brinkmann J., 2004, *MNRAS*, **351**, 1151
 Brown T., Cortese L., Catinella B., Kilborn V., 2018, *MNRAS*, **473**, 1868
 Bruzual G., Charlot S., 2003, *MNRAS*, **344**, 1000
 Calette A. R., Avila-Reese V., Rodríguez-Puebla A., Hernández-Toledo H., Papastergis E., 2018, *RMxAA*, **54**, 443
 Catinella B., et al., 2010, *MNRAS*, **403**, 683
 Catinella B., et al., 2013, *MNRAS*, **436**, 34
 Chabrier G., 2003, *PASP*, **115**, 763
 Cresci G., Mannucci F., Curti M., 2019, *A&A*, **627**, A42
 DESI Collaboration et al., 2016, preprint, ([arXiv:1611.00036](https://arxiv.org/abs/1611.00036))
 Dalcanton J. J., 2007, *ApJ*, **658**, 941
 Davé R., Finlator K., Oppenheimer B. D., 2012, *MNRAS*, **421**, 98
 Davé R., Rafieferantsoa M. H., Thompson R. J., Hopkins P. F., 2017, *MNRAS*, **467**, 115
 Davis M., Peebles P. J. E., 1983, *ApJ*, **267**, 465
 Dayal P., Ferrara A., Dunlop J. S., 2013, *MNRAS*, **430**, 2891

- Ellison S. L., Patton D. R., Simard L., McConnachie A. W., 2008, *ApJL*, 672, L107
- Faber S. M., et al., 2007, *ApJ*, 665, 265
- Fakhouri O., Ma C.-P., 2010, *MNRAS*, 401, 2245
- Foreman-Mackey D., Hogg D. W., Lang D., Goodman J., 2013, *PASP*, 125, 306
- Fu J., Guo Q., Kauffmann G., Krumholz M. R., 2010, *MNRAS*, 409, 515
- Gunn J. E., Gott III J. R., 1972, *ApJ*, 176, 1
- Guo H., Li C., Zheng Z., Mo H. J., Jing Y. P., Zu Y., Lim S. H., Xu H., 2017, *ApJ*, 846, 61
- Haynes M. P., Giovanelli R., Chincarini G. L., 1984, *ARA&A*, 22, 445
- Haynes M. P., et al., 2011, *AJ*, 142, 170
- Haynes M. P., et al., 2018, preprint, ([arXiv:1805.11499](https://arxiv.org/abs/1805.11499))
- Hinshaw G., et al., 2013, *ApJS*, 208, 19
- Hughes T. M., Cortese L., Boselli A., Gavazzi G., Davies J. I., 2013, *A&A*, 550, A115
- Jaffé Y. L., Smith R., Candlish G. N., Poggianti B. M., Sheen Y.-K., Verheijen M. A. W., 2015, *MNRAS*, 448, 1715
- Kannappan S. J., 2004, *ApJ*, 611, L89
- Kashino D., Renzini A., Silverman J. D., Daddi E., 2016, *ApJL*, 823, L24
- Kauffmann G., et al., 2003a, *MNRAS*, 341, 33
- Kauffmann G., et al., 2003b, *MNRAS*, 346, 1055
- Kennicutt R. C., Evans N. J., 2012, *ARA&A*, 50, 531
- Bundy K., et al., 2015, *ApJ*, 798, 7
- Kronberger T., Kapferer W., Ferrari C., Unterguggenberger S., Schindler S., 2008, *A&A*, 481, 337
- Lada C. J., Forbrich J., Lombardi M., Alves J. F., 2012, *ApJ*, 745, 190
- Lara-López M. A., et al., 2010, *A&A*, 521, L53
- Lelli F., McGaugh S. S., Schombert J. M., 2016, *ApJ*, 816, L14
- Leroy A. K., et al., 2013, *AJ*, 146, 19
- Li C., Kauffmann G., Fu J., Wang J., Catinella B., Fabello S., Schiminovich D., Zhang W., 2012, *MNRAS*, 424, 1471
- Li J., Wang Y.-G., Kong M.-Z., Wang J., Chen X., Guo R., 2018, *Research in Astronomy and Astrophysics*, 18, 003
- Liao S., Gao L., 2018, preprint, ([arXiv:1805.10944](https://arxiv.org/abs/1805.10944))
- Lilly S. J., Carollo C. M., Pipino A., Renzini A., Peng Y., 2013, *ApJ*, 772, 119
- Maartens R., Abdalla F. B., Jarvis M., Santos M. G., SKA Cosmology SWG f. t., 2015, preprint, ([arXiv:1501.04076](https://arxiv.org/abs/1501.04076))
- Maddox N., Hess K. M., Obreschkow D., Jarvis M. J., Blyth S.-L., 2015, *MNRAS*, 447, 1610
- Mandelbaum R., Wang W., Zu Y., White S., Henriques B., More S., 2016, *MNRAS*, 457, 3200
- Mannucci F., Cresci G., Maiolino R., Marconi A., Gnerucci A., 2010, *MNRAS*, 408, 2115
- Matteucci F., 2012, *Chemical Evolution of Galaxies*, [doi:10.1007/978-3-642-22491-1](https://doi.org/10.1007/978-3-642-22491-1).
- McCarthy I. G., Frenk C. S., Font A. S., Lacey C. G., Bower R. G., Mitchell N. L., Balogh M. L., Theuns T., 2008, *MNRAS*, 383, 593
- McGaugh S. S., Schombert J. M., Bothun G. D., de Blok W. J. G., 2000, *ApJ*, 533, L99
- Merritt D., 1983, *ApJ*, 264, 24
- Moore B., Katz N., Lake G., Dressler A., Oemler A., 1996, *Nature*, 379, 613
- Nan R., et al., 2011, *International Journal of Modern Physics D*, 20, 989
- Obuljen A., Alonso D., Villaescusa-Navarro F., Yoon I., Jones M., 2018, preprint, ([arXiv:1805.00934](https://arxiv.org/abs/1805.00934))
- Padmanabhan H., Kulkarni G., 2017, *MNRAS*, 470, 340
- Peeples M. S., Shankar F., 2011, *MNRAS*, 417, 2962
- Peeples M. S., Werk J. K., Tumlinson J., Oppenheimer B. D., Prochaska J. X., Katz N., Weinberg D. H., 2014, *ApJ*, 786, 54
- Peng Y.-j., Maiolino R., 2014, *MNRAS*, 438, 262
- Press W. H., Teukolsky S. A., Vetterling W. T., Flannery B. P., 1992, *Numerical recipes in FORTRAN. The art of scientific computing*
- Rafieferantsoa M., Andrianomena S., Davé R., 2018, *MNRAS*, 479, 4509
- Rozo E., Rykoff E. S., 2014, *ApJ*, 783, 80
- Salim S., et al., 2007, *ApJS*, 173, 267
- Salim S., et al., 2007, *ApJS*, 173, 267
- Salim S., Lee J. C., Ly C., Brinchmann J., Davé R., Dickinson M., Salzer J. J., Charlot S., 2014, *ApJ*, 797, 126
- Sánchez S. F., et al., 2013, *A&A*, 554, A58
- Sánchez S. F., et al., 2017, *MNRAS*, 469, 2121
- Sánchez S. F., et al., 2019, *MNRAS*, 484, 3042
- Sancisi R., Fraternali F., Oosterloo T., van der Hulst T., 2008, *A&ARv*, 15, 189
- Simha V., Weinberg D. H., Conroy C., Dave R., Fardal M., Katz N., Oppenheimer B. D., 2014, preprint, ([arXiv:1404.0402](https://arxiv.org/abs/1404.0402))
- Teimoorinia H., Ellison S. L., Patton D. R., 2017, *MNRAS*, 464, 3796
- Telford O. G., Dalcanton J. J., Skillman E. D., Conroy C., 2016, *ApJ*, 827, 35
- Tremonti C. A., et al., 2004, *ApJ*, 613, 898
- Tumlinson J., Peeples M. S., Werk J. K., 2017, *ARA&A*, 55, 389
- Wang E., Kong X., Pan Z., 2018, preprint, ([arXiv:1808.05929](https://arxiv.org/abs/1808.05929))
- Wetzel A. R., Tinker J. L., Conroy C., van den Bosch F. C., 2013, *MNRAS*, 432, 336
- Xie L., De Lucia G., Wilman D. J., Fossati M., Erwin P., Gutierrez L., Kulkarni S. K., 2018, preprint, ([arXiv:1808.01628](https://arxiv.org/abs/1808.01628))
- Yang X., Mo H. J., van den Bosch F. C., Pasquali A., Li C., Barden M., 2007, *ApJ*, 671, 153
- Yates R. M., Kauffmann G., Guo Q., 2012, *MNRAS*, 422, 215
- Yoon I., Rosenberg J. L., 2015, *ApJ*, 812, 4
- York D. G., et al., 2000, *AJ*, 120, 1579
- Zahid H. J., Dima G. I., Kudritzki R.-P., Kewley L. J., Geller M. J., Hwang H. S., Silverman J. D., Kashino D., 2014, *ApJ*, 791, 130
- Zhang W., Li C., Kauffmann G., Zou H., Catinella B., Shen S., Guo Q., Chang R., 2009, *MNRAS*, 397, 1243
- Zhang K., et al., 2019, *SCPMA*, 62, 959506
- Zu Y., Mandelbaum R., 2015, *MNRAS*, 454, 1161
- Zu Y., Mandelbaum R., 2016, *MNRAS*, 457, 4360
- Zu Y., Mandelbaum R., 2018, *MNRAS*, 476, 1637

This paper has been typeset from a $\text{\TeX}/\text{\LaTeX}$ file prepared by the author.